Recent advancement of anti-resonant Hollow-Core fibers for sensing applications

Wenjun Ni, Chunyong Yang, Yiyang Luo, Ran Xia, Ping Lu, Dora Juan Juan Hu, Sylvain Danto, Perry Ping Shum, Lei Wei

photonics

MDPI

Review

Recent Advancement of Anti-Resonant Hollow-Core Fibers for Sensing Applications

Wenjun Ni [1], Chunyong Yang [1,*], Yiyang Luo [2], Ran Xia [3], Ping Lu [3], Dora Juan Juan Hu [4], Sylvain Danto [5], Perry Ping Shum [6] and Lei Wei [7,*]

[1] Hubei Key Laboratory of Intelligent Wireless Communications, Hubei Engineering Research Center of Intelligent Internet of Things Technology, College of Electronics and Information Engineering, South-Central University for Nationalities, Wuhan 430074, China; wjni@mail.scuec.edu.cn
[2] Key Laboratory of Optoelectronic Technology & Systems (Ministry of Education), Chongqing University, Chongqing 400044, China; yyluo@cqu.edu.cn
[3] School of Optical and Electronic Information, Huazhong University of Science and Technology, Wuhan 430074, China; ranxia@hust.edu.cn (R.X.); pluriver@mail.hust.edu.cn (P.L.)
[4] Institute for Infocomm Research, 1 Fusionopolis Way, #21-01 Connexis, Singapore 138632, Singapore; jjhu@i2r.a-star.edu.sg
[5] CNRS, University of Bordeaux, Bordeaux INP, ICMCB, UMR 5026, F-33600 Pessac, France; sylvain.danto@u-bordeaux.fr
[6] Department of Electrical and Electronic Engineering, College of Engineering, Southern University of Science and Technology, Shenzhen 518055, China; shenp@sustech.edu.cn
[7] School of Electrical and Electronic Engineering, Nanyang Technological University, 50 Nanyang Avenue, Singapore 639798, Singapore
* Correspondence: cyyang@mail.scuec.edu.cn (C.Y.); wei.lei@ntu.edu.sg (L.W.)

Citation: Ni, W.; Yang, C.; Luo, Y.; Xia, R.; Lu, P.; Hu, D.J.J.; Danto, S.; Shum, P.P.; Wei, L. Recent Advancement of Anti-Resonant Hollow-Core Fibers for Sensing Applications. *Photonics* **2021**, *8*, 128. https://doi.org/10.3390/photonics8040128

Academic Editor: Carlos Marques

Received: 21 March 2021
Accepted: 15 April 2021
Published: 19 April 2021

Abstract: Specialty fibers have enabled a wide range of sensing applications. Particularly, with the recent advancement of anti-resonant effects, specialty fibers with hollow structures offer a unique sensing platform to achieve highly accurate and ultra-compact fiber optic sensors with large measurement ranges. This review presents an overview of recent progress in anti-resonant hollow-core fibers for sensing applications. Both regular and irregular-shaped fibers and their performance in various sensing scenarios are summarized. Finally, the challenges and possible solutions are briefly presented with some perspectives toward the future development of anti-resonant hollow-core fibers for advanced sensing.

Keywords: specialty fiber; anti-resonant effect; hollow structure; sensing applications

1. Introduction

Optical fiber, as a transmission medium, has enabled the world to move into a rapid and high-capacity communication age. Particularly, ultra-long distance transmission has been made possible by ultralow propagation loss (~0.17 dB/km) of silica fiber [1]. Even so, faster speed, larger capacity, and longer distance have become inevitable trends of communication requirements, particularly concerning 5G and 6G. Thus, a promising fiber is urgently needed to rival or exceed the conventional single-mode fiber (SMF) in transmission performance. Fortunately, anti-resonant hollow-core fibers (AR-HCFs) have the potential to achieve the aforementioned communication goals, due to their lowest attenuation, optical nonlinearity, and chromatic dispersion over a broad bandwidth [2]. Thanks to breakthroughs at the specialty fiber manufacturing level over the past few years, AR-HCFs have gradually become a research hotspot. However, the transmission loss of AR-HCFs over long distances (>50 km) has not been addressed and this limits applications in novel optical fiber communication systems. Therefore, most of the reported research work concerning specialty fibers with hollow structures is concentrated on transmission loss reduction.

Recently, AR-HCFs with variously irregular cladding structures have been designed and fabricated to reduce transmission loss, and the hollow-core nested anti-resonant nodeless fiber (HC-NANF) is the most common [3]. Figure 1 shows the gradually decreasing transmission loss of AR-HCFs in the past five years. In 2015, Walter Belardi from the University of Bath demonstrated the attenuation of hollow-core anti-resonant fiber (HC-ARF) of 175 dB/km at 480 nm [4]. The year after, a hollow-core revolver fiber with a double-capillary reflective cladding was reported by A. F. Kosolapov et al., which reduced the transmission loss to 75 dB/km at 1850 nm [5]. In 2018, Wang et al. proposed a hollow-core conjoined-tube negative-curvature fiber with a low transmission loss of 2 dB/km at 1512 nm and a <16 dB/km bandwidth spanning across the O, E, S, C, L telecom bands (1302–1637 nm) [6]. Subsequently, based on HC-NANF, Thomas D. Bradley et al. achieved lower transmission losses of 1.3 dB/km [7] and 0.65 dB/km [8] corresponding to the transmission distance of 0.5 km and 1.2 km, respectively. Quickly, they reported that using HC-NANF reached the currently lowest attenuation of 0.28 dB/km over the C and L bands [9]. The transmission loss of HC-NANF is approaching the conventional SMF, which is located in the same order of magnitude. Additionally, the nonlinearities of AR-HCFs are 3~4 orders of magnitude lower than SMF, resulting in ultralow dispersion. On the basis of ultralow transmission loss and chromatic dispersion, Lumenisity limited experimentally demonstrated that HC-NANF realized 10 Gbit dense wavelength division multiplexing (DWDM) transmission over 10 km links [10]. Nevertheless, AR-HCF-based novel fiber devices still have a long way to overcome the difficulties of ultra-long transmission distance. Moreover, AR-HCFs also face limitations of volume production and preparation technology. Though AR-HCFs have unsolved issues in fiber communications, they have shone in optical fiber sensing applications owing to their unique anti-resonant effect and inline hollow-core platform.

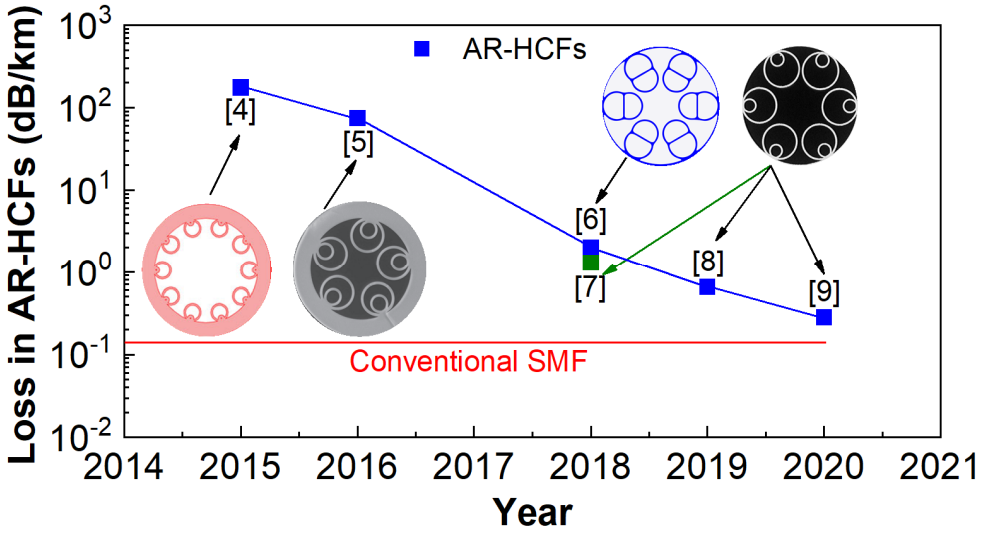

Figure 1. Transmission loss of AR-HCFs in different years.

This article illustrates a comprehensive review of the recent advancement of AR-HCFs for sensing applications. In the past five years, AR-HCFs have been widely employed in the sensing of various physical parameters, including temperature, strain, curvature, displacement, liquid level, and mechanical force, etc. All these measurands fully exploit the intrinsic advantages of anti-resonant effects that can generate specific resonant wavelengths over a broadband window. The sensitivity is then acquired by monitoring the shift or intensity fluctuation of the specific resonant wavelength. Additionally, AR-HCF is also a promising candidate for optofluidic applications because the hollow structure can offer a platform for fluid–light interaction. Consequently, AR-HCFs have attracted more attention for crucial applications in biomedical and biochemical fields, such as the detection of antibiotics, bisphenol, nitrous oxide, methane, and acetylene. Particularly, multiple gas

detection will have significant potential applications in the fields of petrochemical and environmental protection, since AR-HCFs can act as a cell for gas–light interaction over extended lengths. In view of the aforementioned superiorities, AR-HCFs could pave the way for highly accurate, ultracompact, and practical sensing applications. In this text, we present the state-of-the-art of AR-HCF-based sensing applications. Firstly, we introduce the basic principle and some typical structures of AR-HCFs. Section 3 then focuses on recent advancements in sensing applications. Finally, we provide an outlook of development prospects and our related insights and viewpoints.

2. Principle and Various Structure of AR-HCFs

2.1. Principle of Light Propagation in AR-HCFs

In general, AR-HCFs features irregular silica cladding and an air core, which induces a special light propagation path. Here, AR-HCFs obey the light-guiding mechanisms of the anti-resonant reflecting optical waveguide (ARROW) [11], rather than the principle of total internal reflection of SMF. ARROW exploits coherent reflections at the air–silica interface to effectively guide the forward propagation light into the central hollow-core. To intuitively reflect the light propagation in the AR-HCFs, the hollow-core capillary with regular silica cladding is selected as the representative to describe the anti-resonant theory. As shown in Figure 2a, hollow-core capillary with a length L is sandwiched by the two segments of SMFs. The hollow-core capillary with regular ring cladding can be regarded as the FP cavity along the radial direction. The light beams, I_1 and I_2, represent the first reflection of their incident light at the air–silica and silica-air interface, respectively. Here, the incident light of I_2 is the refract light generated by the initial incident light. Then, the two beams I_1 and I_2 will form interference in the air core on the condition that the initial incident angle θ meets the grazing incidence (θ~90°). When the incident light of I_2 reaches the phase matching condition, it will leak out of the cladding. The leaked light is called resonant light, similarly, the reflected part is AR light. In short, AR-HCFs exploit coherent reflections from cladding to confine the guided light and propagate in the central air core. Thus, these light transmission mechanisms reveal the basic principle of the AR effect in HCFs. In addition, it is worth noting that the generation of the AR effect is limited by the length of the HCF. Obviously, if L is short enough, the Fabry–Perot (FP) cavity formed by the two fusion splicing interfaces dominates the whole transmission spectrum, as exhibited in Figure 2b. With an increasing L, however, the FP effect will gradually be weak or disappear caused by the increasing space loss. At this moment, nearly all of the light follows the ARROW transmission mechanisms. It can be seen that a critical length exists between FP and AR effect. The critical length L_c corresponds to the axial transmission length of beam I_2, it can be expressed as follows [12]:

$$L_c = \sqrt{n_0^2 + n_2^2 - n_1^2}\left(\frac{r}{\sqrt{n_1^2 - n_2^2}} + \frac{2d}{\sqrt{n_1^2 - n_0^2}}\right) \quad (1)$$

where n_0, n_1, and n_2 represent the refractive index of air, fiber core of SMF, and cladding, respectively. r and d denote the radius of the air core and the thickness of the ring cladding, respectively. If the capillary length is longer than L_c, the AR effect will be excited in the whole process. Otherwise, the sandwich structure only induces the FP effect. Figure 2b shows that several resonant wavelengths with a periodic distribution that is located in the AR effect-based transmission spectrum. According to the phase matching condition, the resonant wavelength λ_r can be given as follows [13]:

$$\lambda_r = \frac{2\left(d\sqrt{n_2^2 - n_0^2}\right)}{m} \quad (2)$$

where m is the resonance order. All of the aforementioned statements about AR-HCFs are based on the regular shape of the silica cladding, while most of the application scenes

rely on an irregular structure to enhance the sensitivity. In view of diversified sensing applications, the next part will accordingly introduce the various structure of AR-HCFs.

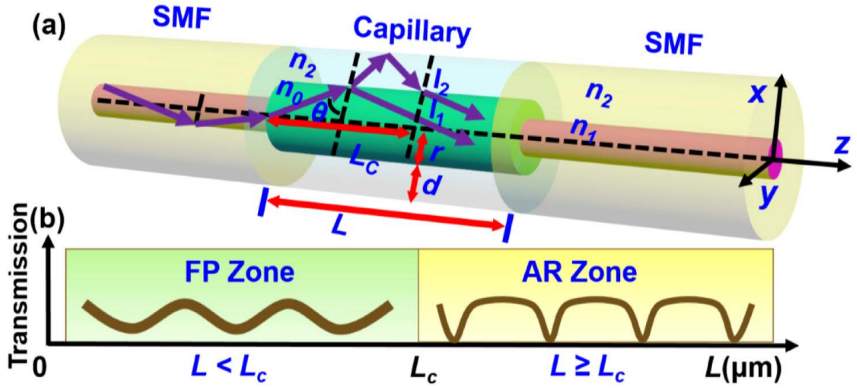

Figure 2. Schematic illustration of (**a**) optical pathways in the SMF–capillary–SMF structure and (**b**) transmission spectra as the increase of capillary length. [Reprinted/Adapted] with permission from [12] © The Optical Society.

2.2. Various Structures of AR-HCFs

In the past decade, AR-HCFs have experienced rapid development, mainly concentrated on structure improvement. The simplest structure is the hollow-core capillary exhibited in Figure 2a; thus, it is regarded as fundamental to exploiting novel structures. The optimization progress can be generally divided into three stages. Firstly, the negative curvature core [14] with a dense arrangement is introduced to surround the air core [15–18], as presented in Figure 3a. Then, several capillary tubes are designed to suspend on the silica cladding to form a negative curvature structure [19–30], as shown in Figure 3b. Finally, the suspended capillary tubes are optimized to be nested structures, as displayed in Figure 3c,d. In this way, the number of coherent reflections at the air–silica interface is increased and, thus, confinement loss is reduced, which is the latest HC-NANF [31,32].

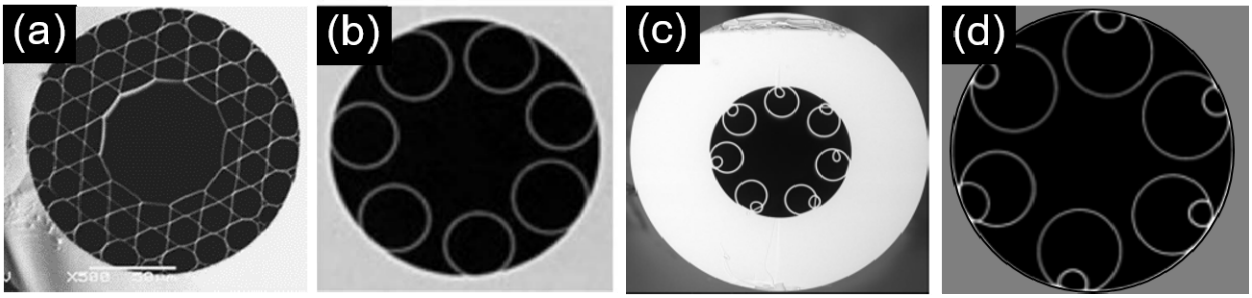

Figure 3. Scanning electron micrographs (SEMs) of AR-HCFs. (**a**) [Reprinted/Adapted] with permission from [16] © The Optical Society. (**b**) © 2017 IEEE. Reproduced with permission from Hayes et al., J. Lightwave Technol. 35, 437–442 (2017) [22]. (**c**) © 2017 IEEE. Reproduced with permission from Jose E. Antonio-Lopez et al., IEEE Photonics Conference (2017) [31]. (**d**) © 2020 IEEE. Reproduced with permission from Y. Hong, J. Lightwave Technol. 38, 2849–2857 (2020) [32].

All these AR-HCFs utilize the negative curvature effect in the surrounding region of the central core to reduce attenuation and promote longer propagation distance, so they are also referred to as negative curvature fibers (NCF). In other words, in most cases, AR-HCFs focus the performance enhancement on the optimization of negative curvature structure. In general, the performance of novel structures depends on significant indicator parameter improvements after optimization. Accordingly, Table 1 lists several key parameters of various AR-HCFs as contrasts.

Table 1. Parameters in various AR-HCFs.

Type	Core Diameter	Silica Thickness	Transmission Loss	Reference
Densely arrangement	45.8 μm	0.51 μm	300 dB/km	[15]
	50 μm	0.28 μm	180 dB/km	[16]
	60 μm	1.4 μm	17 dB/km	[18]
Suspended capillary tubes	30 μm	0.44 μm	180 dB/km	[19]
	30 μm	0.83 μm	30 dB/km	[21]
	41 μm	0.545 μm	7.7 dB/km	[26]
Nested Suspended tubes	25 μm	2.3 μm	75 dB/km	[5]
	~33 μm	~0.78 μm	2 dB/m	[31]
	~35 μm	~0.5 μm	6.6 dB/km	[32]

Table 1 illustrates that the silica thickness is one or two orders of magnitude lower than the core diameter. Here, the geometric size of the air core and silica cladding are in accordance with the AR theory in Section 2.1. Meanwhile, it can be seen from Table 1 that the transmission loss of various AR-HCFs is gradually decreasing with optimization stages approaching the nested topological structure. Indeed, the latest HC-NANFs based on nested structures achieve low attenuation in wide bandwidth ranges, single-mode transmission in hollow-core regions, and relatively long-distance propagation (~10 km) [10]. Currently, most sensing applications are limited by the aforementioned advantages, and, on the contrary, they require high loss structure modification, multimode coexistence, and micro or small size. It is obvious from Figure 3 that the most popular AR-HCFs still concentrate on the type of suspended capillary tubes. On the one hand, they have appropriate transmission loss values that can be satisfied in most sensing application scenarios [33–39]. On the other hand, their distinct advantage is that they can offer a versatile multichannel and lab-on-a-fiber platform [40–45]. As a consequence, the following sections will emphasize the novel and advanced sensing applications based on the most common AR-HCFs at present.

3. AR-HCF-Based Sensing Applications

Concerning the diversified sensing applications of AR-HCFs, not only can they be defined as discrete specialty fiber sensing devices, but can also be treated as a versatile platform for lab-on-a-fiber. The former is mainly used for common physical or chemical measurand detection, which is also the most reported field. The latter pays more attention to biomedical or online fluidic applications, which are relatively frontier research fields for now. All of the mentioned sensing application mechanisms can be broadly classified into two types, namely, special devices and versatile platforms. Thus, we will discuss the AR-HCF-based sensing applications in the light of these classifications.

3.1. Special Device-Based Sensing Applications

Similar to the Bragg wavelength for fiber Bragg grating (FBG) [46–48] and loss peak for long period grating (LPG) [49,50], the resonant wavelength is a remarkable characterization for AR-HCFs. Accordingly, AR-HCFs can be also regarded as one of the functional fiber sensing devices. As analyzed in Section 2.1, the unique AR effect can provide a series of resonant wavelengths with the periodic distribution. The measurand sensitivity can be acquired by interrogating the wavelength shift or intensity. In recent years, most research works have reported sensing applications for generic parameters, including strain, displacement, curvature, static pressure, temperature, liquid level, and mechanical force, et al. Moreover, some modified structures based on AR-HCFs can achieve the simultaneous measurement of dual or multiple parameters. Figure 4 provides a comprehensive review of various sensing applications based on single- or double-layer AR effects.

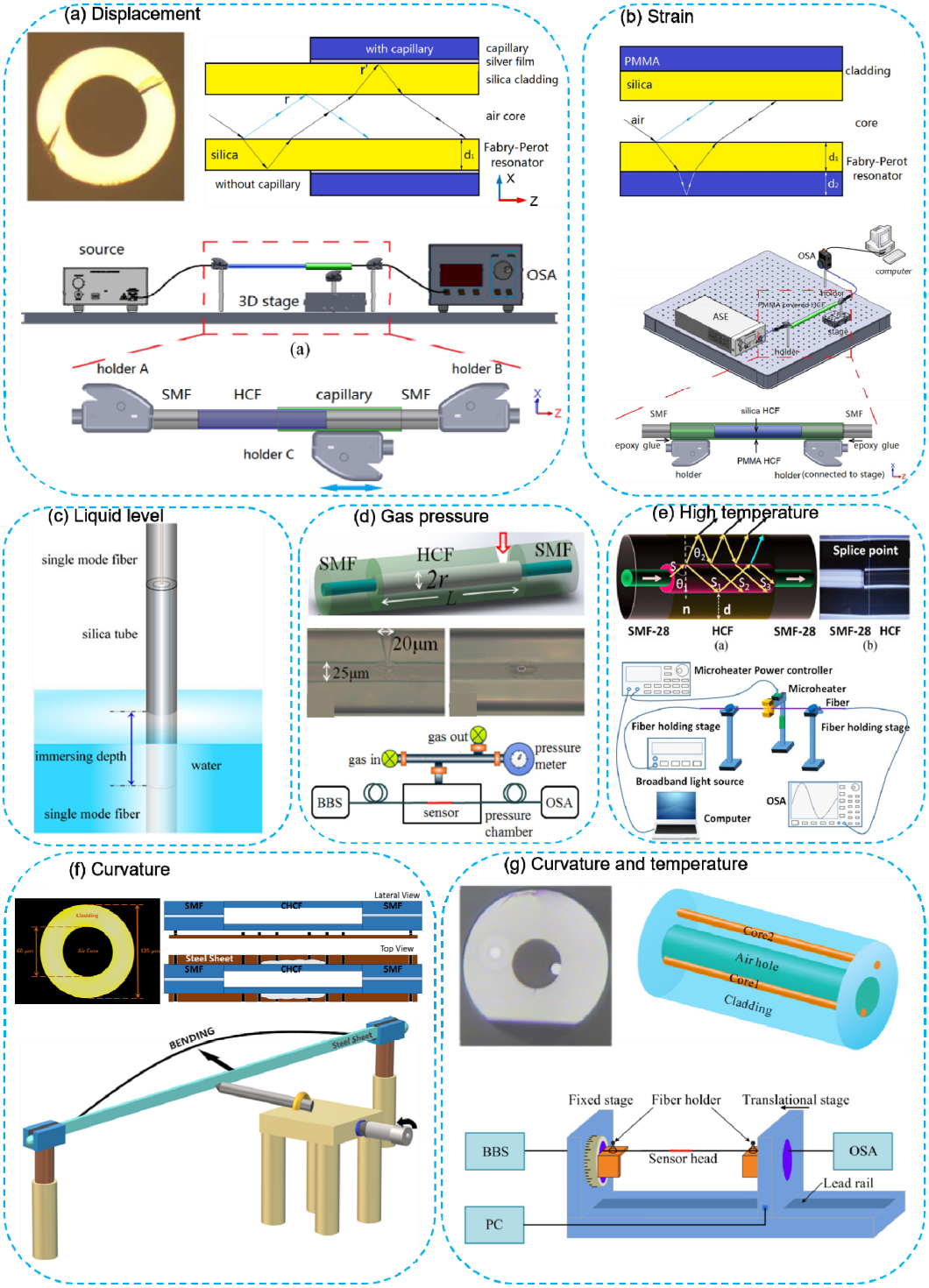

Figure 4. Special device-based sensing applications. (**a**) © 2016 IEEE. Reproduced with permission from R. Gao, J. Sel. Top Quant. 23, 5,600,106 (2016) [51]. (**b**) © 2017 IEEE. Reproduced with permission from R. Gao, IEEE Photonic. Tech. L. 29, 857-860 (2017) [52]. (**c**) © 2015 IEEE. Reproduced with permission from S. Liu, J. Lightwave Technol. 33, 5239-5243 (2016) [53]. (**d**) [Reprinted/Adapted] with permission from [54] © The Optical Society. (**e**) © 2018 IEEE. Reproduced with permission from D. Liu, J. Lightwave Technol. 36, 1583-1590 (2018) [55]. (**f**) Reproduced with permission [56]. Copyright 2020 MDPI. (**g**) [Reprinted/Adapted] with permission from [57] © The Optical Society.

Figure 4a shows that the inner capillary is coated with silver, and then wraps the HCF [51]. This most common HCF agrees with the theory of Section 2.1, so it will form an FP cavity in the cladding. The leaky mode of the HCF actually features the resonant

wavelengths in the transmission spectrum. The initial leaky mode will be reflected back into cladding with the capillary location movement because the covered part is transformed to the silica–silver interface. Thus, the intensity of the resonant wavelength is sensitive to the displacement, and it finally obtains a high sensitivity of 0.578 dB/μm. Likewise, as shown in Figure 4b, HCF is inserted into the polymethyl methacrylate (PMMA) hollow-core fiber [52]. This is a double-layer AR structure since the refractive index of PMMA is between air and silica. The distinct difference between the single- and double-layer AR structure is the free spectrum range (FSR), and the latter is larger than the former owing to the longer optical path. The tensile strain will reduce the thickness of the PMMA resulted in the optical path change, then the resonant wavelength will shift. Using this double-layer AR structure, it achieves the strain sensitivity of 27.9 pm/με. As shown in Figure 4c, the HCF is used for liquid level monitoring [53], and the sensing mechanism is similar to that in Figure 4a. The leaky mode intensity is influenced by the change of the surrounding refractive index. More specifically, the contrast of resonant wavelength will increase or decrease with the liquid level rising or falling. On the basis of this simple HCF structure, a liquid-level sensitivity of 0.4 dB/mm has been realized. Furthermore, the temperature cross-sensitivity is only 0.004 mm/°C, which can be regarded as insensitive. It is apparent that all the sensing mechanisms from Figure 4a to Figure 4c are based on the external refractive index change. On the contrary, Figure 4d devotes to the inner refractive index variation to induce the wavelength shift [54]. As displayed in Equation (2), the resonant wavelength not only depends on the silica thickness and refractive index, but also the air core refractive index. It exploits femtosecond laser drilling on the ring cladding to form a microchannel, which keeps the air-core pressure equivalent to the external environment. The manufactured part is placed into the airtight container, then the increasing pressure will induce the air core refractive index change. The gas pressure sensitivity reaches 3.592 nm/MPa by the wavelength demodulation in the range of 0 to 2 MPa. It can be seen from Figure 4a to Figure 4d, that they only cause a single parameter change in the whole sensing process, and all of these structures transfer to the refractive index variation. While temperature is treated as a sensing variable, which can simultaneously induce parameter changes in multiple structures in the AR-HCFs. As shown in Figure 4e, HCF is applied to high-temperature measurement attributed to the AR effect [55]. It is difficult to use common multimode interference for high-temperature sensing because the employed high order cladding modes have a nonlinearity variation with the temperature increasing. For the HCF, the AR effect is only dependent on the geometric size and material refractive index. Thereby, AR-HCFs have a linear relationship with temperature in a large dynamic range. Figure 4e shows a high-temperature sensitivity of 33.4 pm/°C with the working range from room temperature to 1000 °C. The sensitivities of all the aforementioned structures are determined by their own material properties. Figure 4f enhances the curvature sensitivity assisted by coating the sensitive material [56]. After the polydimethylsiloxane (PDMS) coated on the HCF, the mode confinement is reduced and bending losses are significantly higher. By the external structure modifications, it acquires the curvature sensitivity of -5.26 dB/m^{-1}, which is several times higher than without PDMS coated. In addition, the structure modifications can be also conducted by the special design of HCF. Figure 4g illustrates a novel fiber with a single-hole twin eccentric core, which simultaneously has AR effect and inline Mach-Zehnder interference (IMMI) functions [57]. In this case, the dual or multiple parameters can be measured simultaneously based on different mechanisms and without crosstalk. A curvature sensitivity of -1.54 dB/m^{-1} and the temperature sensitivity of 70.71 pm/°C is realized based on the AR effect and IMMI, respectively. The listed seven examples reveal that the most common HCF mainly rely on the AR effect for sensing at present.

In summary, AR effect-based HCFs have been widely used for all kinds of sensing applications, covering solids, gas, and liquid. Among the AR-HCFs, some have been used for practical applications. Nonetheless, the detection of most parameters is part of mechanisms research, and, thus, remains at a laboratory stage.

3.2. Versatile Platform Based Sensing Applications

The HCFs in 3.1 are relatively simple structures without negative curvature topological configurations. This section introduces AR-HCFs with negative curvature structures. Here, the dominant AR effect, like the Figure 4 examples, will still exist in the irregular hollow-core region. The AR-HCFs in this section mainly exploit the multichannel structure for fluidic sensing. In contrast to common HCFs, these AR-HCFs need to fill various gases, liquids, or solid materials in the air channel to enhance the light–matter interaction. This versatile platform can offer a promising route for compact, integral, and biocompatible all-fiber multifunctional optofluidic devices for in-situ applications.

As shown in Figure 5a, light is guided inside an air core filled with the analyte gas, and the AR-HCF serves as a low-volume and robust absorption cell. Laser-based gas sensors utilize borosilicate fiber because the absorption wavelength of the monitoring nitrous oxide is located at 5.26 µm. The feasibility of exploiting the eight-hole AR-HCF with 1.15 m length as a gas cell is verified, and the minimum detection limitation (MDL) of 20 ppbv with 70 s signal interrogation time is achieved [58]. Similarly, Figure 5b replaces the eight-hole negative curvature with a nested nodeless structure for nitrous oxide sensing [59]. Compared with Figure 5a, the whole length of AR-HCF is increased to 3.2 m, so the time and area of light–gas interaction is accordingly enhanced. Finally, the experimental results show that the response time shortens to 1s and the MDL decreases to ~5.4 ppbv. Figures 5a and 5b are used for single gas detection, which is a waste of resources. In practical applications, most occasions require simultaneous measurement of multi-component gas, for example, gas micro-leakage in a transformer. As shown in Figure 5c, laser-based dual gas sensing of methane and carbon dioxide is achieved by a length of 1m silica AR-HCF. The absorption wavelengths of these two gasses are 3.334 µm and 1.574 µm, respectively, corresponding to the near- and mid-infrared spectral region [60]. That is, the monitoring crosstalk between methane and carbon dioxides can be well avoided, which paves the way for multi-component gas detection. The experimental results show that the MDL of methane and carbon reaches 24 ppbv and 144 ppmv, respectively. From Figure 5a to Figure 5c, all the utilized AR-HCFs retain the single-mode transmission in the air core region. In order to acquire lower MDL, Figure 5d demonstrates a mode-phase-difference (MPD) photothermal spectroscopy for acetylene detection [61]. In a 4-m-long AR-HCF, it supports LP_{01}-like and LP_{11}-like transmission in a broadband. The photothermal effect induces variations of the dual-mode refractive index. The MPD is sensitive to gas absorption and insensitive against the external environment perturbation. The proof-of-concept realizes the MDL down to pptv. AR-HCFs are treated as microcells to provide a gas–light interaction platform in the aforementioned four examples. More importantly, AR-HCFs have a great potential for multi-component gas simultaneous detection owing to the wide transmission broadband in the air core region, nearly covering all molecule absorption lines. In addition to gas detection, AR-HCFs are also attracting attention for their potential in liquid sensing. The distinct difference of absorption spectroscopy measurements between gas and liquid is the different filling medium. As shown in Figure 5e, the hollow-core region is filled with antibiotic, which will cause the absorption of the guided light. Using a 1-m-long AR-HCF achieves the detection of sulfamethoxazole (SMX) and sodium salicylate (SS) down to 0.1 µM (26 ppb) and 0.4 µM (64 ppb), respectively [62]. Figure 5f conducts a proof-of-concept experiment of Raman spectroscopy using ethanol, which provides an original idea for noninvasive biochemical analysis [63]. In contrast to Figure 5e–g principally proposes a low-loss micro-machining method for optofluidic applications [64]. They exploit the focused ion beam to mill the cladding of AR-HCFs, and no additional loss is generated in the whole process. Once the hole of the cladding is opened, it will shine new light on the inline optofluidic applications. This method is similar to femtosecond laser drilling on the ring cladding in Figure 4d. Both contribute to forming the inline channel. Figure 5h utilizes a 40-cm-long AR-HCF to reach the MDL of 1.69 pM for bisphenol A detection [65], which is the experimental verification for Figure 5f. The applications depicted in Figure 5a–h are all employed in fluidic detection, including gas and liquid. While in Figure 5i, HC-NANF is wound into

a coil to be integrated into a resonator fiber optic gyroscope [66]. This structure not only breaks through the limitation of nonlinear influence, but also considerably improves spatial mode purity. It is a promising candidate for civil aircraft navigation usage. In recent years, some AR-HCF-based optofluidic applications have been used for practical applications based on similar methods developed for microstructured fiber-based devices [67–72].

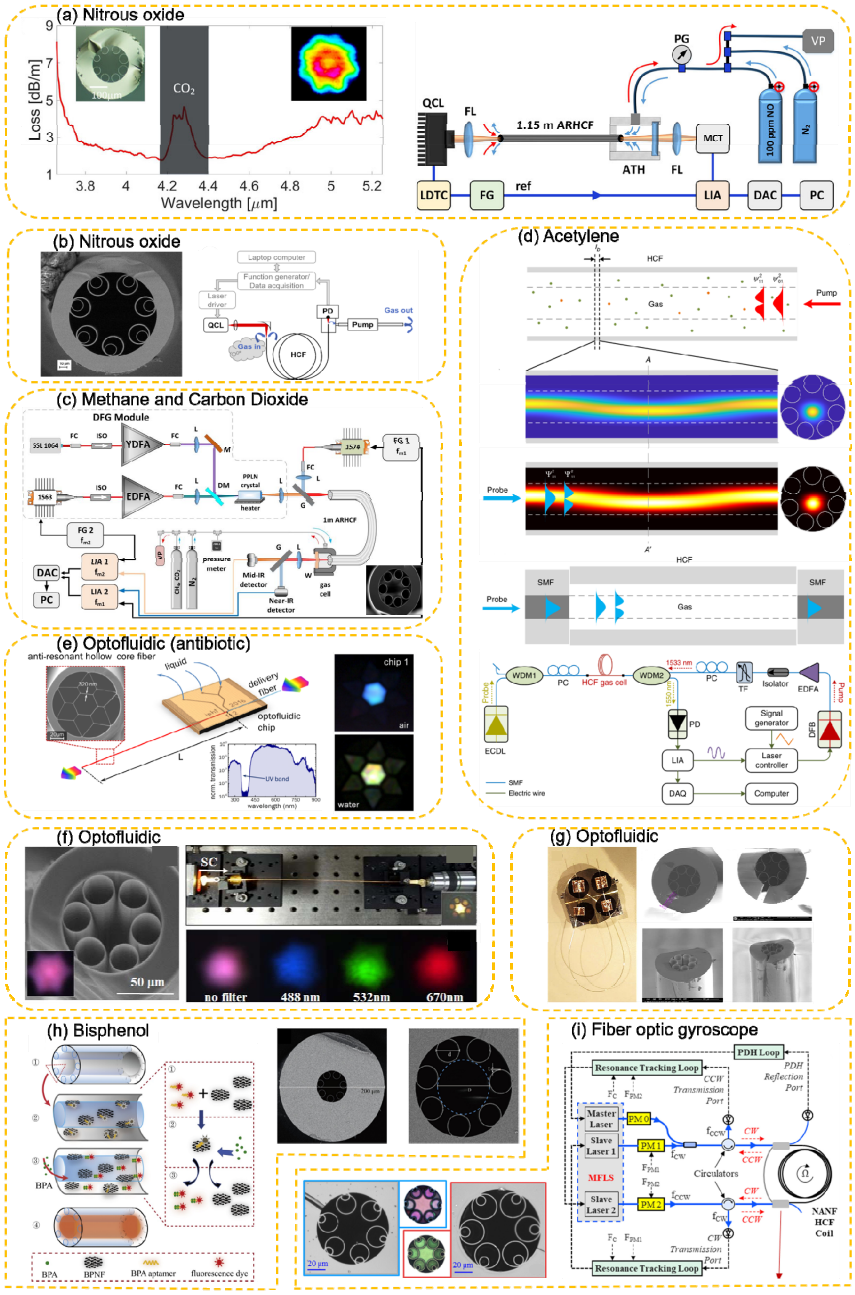

Figure 5. Versatile platform based sensing applications. (**a**) [Reprinted/Adapted] with permission from [58] © The Optical Society. (**b**) [Reprinted/Adapted] with permission from [59] © The Optical Society. (**c**) Reproduced with permission [60]. Copyright 2020 MDPI. (**d**) Reproduced with permission [61]. Copyright 2020, Springer Nature. (**e**) Reproduced with permission [62]. Copyright 2018 MDPI. (**f**) [Reprinted/Adapted] with permission from [63] © The Optical Society. (**g**) [Reprinted/Adapted] with permission from [64] © The Optical Society. (**h**) Reproduced with permission [65]. Copyright 2020, Elsevier. (**i**) [Reprinted/Adapted] with permission from [66] © The Optical Society.

4. Prospects and Conclusions

Enabled by the specialty fiber manufacturing industry, AR-HCFs have shown great potential in optical fiber communication and sensing. AR-HCFs have very low transmission loss, optical nonlinearity, and chromatic dispersion over a broad bandwidth. They also have intrinsic advantages of high sensitivity, compact structures, and robust operation. All these remarkable advantages promote diversified sensing applications of AR-HCF. As a functionalized device, it has been extensively used for common parameter sensing, including solid, gas, and liquid. Meanwhile, as a versatile platform, it sheds new light on optofluidic fields, mainly including gas micro-leakage, multi-component gas, pharmaceutical substances, and tissue fluid detection. Particularly, the versatile platform has made a significant contribution to providing a new route for photoacoustic spectroscopy (PAS) or photothermal spectroscopy (PTS). With the rapid development of micro-machining techniques, there have been substantial laboratory-stage research achievements, inspiring hope for practical applications. Furthermore, it is believed that AR-HCF will become the ultimate optical fiber once there has been a breakthrough in long-distance single-mode transmission loss.

Author Contributions: W.N. and L.W. contributed to the idea. W.N. contributed to the writing of the manuscript. W.N., C.Y., Y.L., R.X., P.L., D.J.J.H., S.D., P.P.S. and L.W. contributed to the reviewing and editing of the manuscript. C.Y. and L.W. supervised the project. All authors have read and agreed to the published version of the manuscript.

Funding: This work was supported by the Key Technology R&D Program of Hubei province under Grant 2020BBB097, Singapore Ministry of Education Academic Research Fund Tier 2 (MOE2019-T2-2-127 and T2EP50120-0005), A*STAR under AME IRG (A2083c0062), the Singapore Ministry of Education Academic Research Fund Tier 1 (RG90/19 and RG73/19) and the Singapore National Research Foundation Competitive Research Program (NRF-CRP18-2017-02). This work was also supported by South-Central University for Nationalities and Nanyang Technological University.

Data Availability Statement: Data sharing not applicable.

Conflicts of Interest: The authors declare no conflict of interest.

References

1. Sagae, Y.; Matsui, T.; Sakamoto, T.; Nakajima, K. Ultra-Low Crosstalk Multi-Core Fiber with Standard 125-μm Cladding Diameter for 10,000km-Class Long-Haul Transmission. *IEICE Trans. Commun.* **2020**, *E103.B*, 1199–1205. [CrossRef]
2. Habib, M.S.; Bang, O.; Bache, M. Low-loss single-mode hollow-core fiber with anisotropic anti-resonant elements. *Opt. Express* **2016**, *24*, 8429–8436. [CrossRef]
3. Francesco, P. Nested antiresonant nodeless hollow core fiber. *Opt. Express* **2014**, *22*, 23807–23828.
4. Belard, W. Design and Properties of Hollow Antiresonant Fibers for the Visible and Near Infrared Spectral Range. *J. Lightwave Technol.* **2015**, *33*, 4497–4503. [CrossRef]
5. Kosolapov, A.F.; Alagashev, G.K.; Kolyadin, A.N.; Pryamikov, A.D.; Biryukov, A.S.; Bufetov, I.A.; Dianov, E.M. Hollow-core revolver fibre with a double-capillary reflective cladding. *Quantum Electron.* **2016**, *46*, 267–270. [CrossRef]
6. Gao, S.; Wang, Y.; Ding, W.; Jiang, D.; Gu, S.; Zhang, X.; Wang, P. Hollow-core conjoined-tube negative-curvature fibre with ultralow loss. *Nat. Commun.* **2018**, *9*, 1–6. [CrossRef]
7. Bradley, T.D.; Hayes, J.R.; Chen, Y.; Jasion, G.T.; Sandoghchi, S.R.; Slavik, R.; Fokoua, E.N.; Bawn, S.; Sakr, H.; Davidson, I.A.; et al. Record low-loss 1.3 dB/km data transmitting antiresonant hollow core fibre. In Proceedings of the 2018 European Conference on Optical Communication (ECOC), Rome, Italy, 23–27 September 2018.
8. Bradley, T.D.; Jasion, G.T.; Hayes, J.R.; Chen, Y.; Hooper, L.; Sakr, H.; Gouveia, M.A.; Taranta, A.; Saljoghei, A.; Mulvad, H.C.; et al. Antiresonant hollow core fibre with 0.65 dB/km attenuation across the C and L telecommunication bands. In Proceedings of the 45th European Conference on Optical Communication (ECOC 2019), Dublin, Ireland, 22–26 September 2019.
9. Jasion, G.T.; Bradley, T.D.; Harrington, K.; Sakr, H.; Chen, Y.; Fokoua, E.N.; Davidson, I.A.; Taranta, A.; Hayes, J.R.; Richardson, D.J.; et al. Hollow core NANF with 0.28 dB/km attenuation in the C and L bands. In Proceedings of the Optical Fiber Communication Conference, San Diego, CA, USA, 10–12 March 2020; Optical Society of America: Washington, DC, USA, 2020.
10. Laser Focus World Reported on 01 Oct, 2020, and Sources from Lumenisty Company. Available online: https://www.laserfocusworld.com/fiber-optics/article/14184480/lumenisity-unveils-hollowcore-fiberoptic-cable-for-10-gbit-dwdm-transmission-over-10-km-links (accessed on 14 April 2021).
11. Litchinitser, N.M.; Abeeluck, A.K.; Headley, C.; Eggleton, B.J. Antiresonant reflecting photonic crystal optical waveguides. *Opt. Lett.* **2002**, *27*, 1592–1594. [CrossRef]

12. Xiaobei, Z.; Haiyang, P.; Huawen, B.; Ming, Y.; Jiawei, W.; Chuanlu, D.; Tianxing, W. Transition of Fabry–Perot and antiresonant mechanisms via a SMF-capillary-SMF structure. *Opt. Lett.* **2018**, *43*, 2268–2271.
13. Cai, N.; Xia, L.; Wu, Y. Multiplexing of anti-resonant reflecting optical waveguides for temperature sensing based on quartz capillary. *Opt. Express* **2018**, *26*, 33501–33509. [CrossRef]
14. Wei, C.; Weiblen, R.J.; Menyuk, C.R.; Hu, J. Negative curvature fibers. *Adv. Opt. Photonics* **2017**, *9*, 504–561. [CrossRef]
15. Couny, F.; Benabid, P.S. Light. Large-pitch kagome-structured hollow-core photonic crystal fiber. *Opt. Lett.* **2006**, *31*, 3574–3576. [CrossRef] [PubMed]
16. Wang, Y.Y.; Wheeler, N.V.; Couny, F.; Roberts, P.J.; Benabid, F. Low loss broadband transmission in hypocycloid-core Kagome hollow-core photonic crystal fiber. *Opt. Lett.* **2011**, *36*, 669–671. [CrossRef] [PubMed]
17. Wheeler, N.V.; Heidt, A.M.; Baddela, N.K.; Fokoua, E.N.; Hayes, J.R.; Sandoghchi, S.R.; Poletti, F.; Petrovich, M.N.; Richardson, D.J. Low-loss and low-bend-sensitivity mid-infrared guidance in a hollow-core–photonic-bandgap fiber. *Opt. Lett.* **2014**, *39*, 295–298. [CrossRef]
18. Debord, B.; Alharbi, M.; Bradley, T.; Fourcade-Dutin, C.; Wang, Y.Y.; Vincetti, L.; Gérôme, F.; Benabid, F. Hypocycloid-shaped hollow-core photonic crystal fiber Part I: Arc curvature effect on confinement loss. *Opt. Express* **2013**, *21*, 28597–28608. [CrossRef]
19. Uebel, P.; Günendi, M.C.; Frosz, M.H.; Ahmed, G.; Edavalath, N.N.; Ménard, J.M.; Russell P. St., J. Broadband robustly single-mode hollow-core PCF by resonant filtering of higher-order modes. *Opt. Lett.* **2016**, *41*, 1961–1964. [CrossRef]
20. Provino, L.; Haboucha, A.; Havranek, M.; Monteville, A.; Landais, D.; Goffic, O.; Insou, X.; Barbier, M.; Chartier, T.; Thual, M.; et al. Large-Core Hollow-Core Antiresonant Fiber with Low-Loss and Truly Single-Mode Guidance for N-IR Wavelengths. In Proceedings of the OSA Laser Congress, Boston, MA, USA, 4–8 November 2018; Optical Society of America: Washington, DC, USA, 2018.
21. Michieletto, M.; Jens, K.; Lyngsø, C.J.; Lægsgaard, J.; Bang, O.; Alkeskjold, T.T. Hollow-core fibers for high power pulse delivery. *Opt. Express* **2016**, *24*, 7103–7119. [CrossRef]
22. Hayes, J.R.; Sandoghchi, S.R.; Bradley, T.D.; Liu, Z.; Slavík, R.; Gouveia, M.A.; Wheeler, N.V.; Jasion, G.; Chen, Y.; Fokoua, E.N.; et al. Antiresonant Hollow Core Fiber with an Octave Spanning Bandwidth for Short Haul Data Communications. *J. Lightwave Technol.* **2017**, *35*, 437–442. [CrossRef]
23. Pryamikov, A.D.; Biriukov, A.S.; Kosolapov, A.F.; Plotnichenko, V.G.; Semjonov, S.L.; Dianov, E.M. Demonstration of a waveguide regime for a silica hollow—core microstructured optical fiber with a negative curvature of the core boundary in the spectral region > 3.5 µm. *Opt. Express* **2011**, *19*, 1441–1448. [CrossRef] [PubMed]
24. Kolyadin, A.N.; Kosolapov, A.F.; Pryamikov, A.D.; Biriukov, A.S.; Plotnichenko, V.G.; Dianov, E.M. Light transmission in negative curvature hollow core fiber in extremely high material loss region. *Opt. Express* **2013**, *21*, 9514–9519. [CrossRef]
25. Newkirk, A.V.; Antonio-Lopez, J.E.; Anderson, J.; Aguirre, R.A.; Eznaveh, Z.S.; Galmiche, G.L.; Correa, R.A.; Schülzgen, A. Modal analysis of antiresonant hollow core fibers using S2 imaging. *Opt. Lett.* **2016**, *41*, 3277–3280. [CrossRef]
26. Debord, B.; Amsanpally, A.; Chafer, M.; Baz, A.; Maurel, M.; Blondy, J.M.; Hugonnot, E.; Scol, F.; Vincetti, L.; Gérome, F.; et al. Ultralow transmission loss in inhibited-coupling guiding hollow fibers. *Optica* **2017**, *4*, 209–217. [CrossRef]
27. Belardi, W.; Knight, J.C. Hollow antiresonant fibers with low bending loss. *Opt. Express* **2014**, *22*, 10091–10096. [CrossRef] [PubMed]
28. Kosolapov, A.F.; Pryamikov, A.D.; Biriukov, A.S.; Shiryaev, V.S.; Astapovich, M.S.; Snopatin, G.E.; Plotnichenko, V.G.; Churbanov, M.F.; Dianov, E.M. Demonstration of CO_2-laser power delivery through chalcogenide-glass fiber with negative-curvature hollow core. *Opt. Express* **2011**, *19*, 25723–25728. [CrossRef] [PubMed]
29. Gattass, R.R.; Rhonehouse, D.; Gibson, D.; McClain, C.C.; Thapa, R.; Nguyen, V.Q.; Bayya, S.S.; Weiblen, R.J.; Menyuk, C.L.; Shaw, B.; et al. Infrared glass-based negative-curvature anti-resonant fibers fabricated through extrusion. *Opt. Express* **2016**, *24*, 25697–25703. [CrossRef] [PubMed]
30. Setti, V.; Vincetti, L.; Argyros, A. Flexible tube lattice fibers for terahertz applications. *Opt. Express* **2013**, *21*, 3388–3399. [CrossRef]
31. Antonio-Lopez, J.E.; Habib, M.S.; Newkirk, A.V.; Galmiche, G.L.; Eznaveh, Z.S.; Zacarisa, J.C.; Bang, O.; Bache, M.; Schülzgen, A.; Correa, R.A. Antiresonant hollow core fiber with seven nested capillaries. In Proceedings of the 2016 IEEE Photonics Conference (IPC), Waikoloa, HI, USA, 2–6 October 2016.
32. Hong, Y.; Sakr, H.; Taengnoi, N.; Bottrill, K.R.; Bradley, T.D.; Hayes, J.R.; Jasion, G.T.; Kim, H.; Thipparapu, N.K.; Wang, Y.; et al. Multi-Band Direct-Detection Transmission Over an Ultrawide Bandwidth Hollow-Core NANF. *J. Lightwave Technol.* **2020**, *38*, 2849–2857. [CrossRef]
33. Wang, S.; Shan, C.; Jiang, J.; Liu, K.; Zhang, X.; Han, Q.; Lei, J.; Xiao, H.; Liu, T. Temperature-insensitive curvature sensor based on anti-resonant reflection guidance and Mach–Zehnder interferometer hybrid mechanism. *Appl. Phys. Express* **2019**, *12*, 106503. [CrossRef]
34. Liu, S.; Ji, Y.; Cui, L.; Sun, W.; Yang, J.; Li, H. Humidity-insensitive temperature sensor based on a quartz capillary anti-resonant reflection optical waveguide. *Opt. Express* **2017**, *25*, 18929–18939. [CrossRef]
35. Gao, R.; Lu, D.; Cheng, J.; Qi, Z. Self-referenced antiresonant reflecting guidance mechanism for directional bending sensing with low temperature and strain crosstalk. *Opt. Express* **2017**, *25*, 18081–18091. [CrossRef]
36. Wang, S.; Wang, S.; Zhang, S.; Feng, M.; Wu, S.; Jin, R.; Zhang, L.; Lu, P. An inline fiber curvature sensor based on anti-resonant reflecting guidance in silica tube. *Opt. Laser Technol.* **2019**, *111*, 407–410. [CrossRef]

37. Gao, H.; Jiang, Y.; Zhang, L.; Cui, Y.; Jiang, Y.; Jia, J.; Jiang, L. Antiresonant mechanism based self-temperature-calibrated fiber optic Fabry–Perot gas pressure sensors. *Opt. Express* **2019**, *27*, 22181–22189. [CrossRef] [PubMed]
38. Suo, X.; Yu, H.; Li, J.; Wu, X. Transmissive resonant fiber-optic gyroscope employing Kagome hollow-core photonic crystal fiber resonator. *Opt. Lett.* **2020**, *45*, 2227–2230. [CrossRef] [PubMed]
39. Ni, W.; Lu, P.; Fu, X.; Sun, H.; Shum, P.; Liao, H.; Jiang, X.; Liu, D.; Yang, C.; Zhang, J.; et al. Simultaneous implementation of enhanced resolution and large dynamic range for fiber temperature sensing based on different optical transmission mechanisms. *Opt. Lett.* **2018**, *26*, 18341–18350. [CrossRef]
40. Ankan, I.M.; Mollah, M.A.; Sultana, J.; Islam, M. Negative Curvature Hollow-core Anti-resonant Fiber for Terahertz Sensing. *Appl. Opt.* **2020**, *59*, 8519–8525. [CrossRef]
41. Gao, R.; Lu, D.; Cheng, J.; Jiang, Y.; Jiang, L.; Ye, J.; Qi, Z. Magnetic Fluid-Infiltrated Anti-Resonant Reflecting Optical Waveguide for Magnetic Field Sensing Based on Leaky Modes. *J. Lightwave Technol.* **2016**, *34*, 3490–3495. [CrossRef]
42. Newkirk, A.V.; Lopez, J.E.A.; Correa, R.A.; Schülzgen, A.; Mazurowski, J. Anti-resonant hollow core fiber for precision timing applications. In *Astronomical Optics: Design, Manufacture, & Test of Space & Ground Systems*; Astronomical Optics: San Diego, CA, USA, 2017; Volume 10401, p. 104010F-1.
43. Jaworski, P.; Yu, F.; Boj, P.; Wu, D.; Koziol, P.E.; Dudzik, G.; Abramski, K.M.; Liao, M.; Krzempek, K. Antiresonant Hollow-Core Fiber for Multiple Gas Detection in the Mid-IR. In *CLEO: QELSFundamental Science*; Optical Society of America: Washington, DC, USA, 2020; p. JTu2G.33.
44. Liu, S.; Wang, Y.; Hou, M.; Guo, J.; Li, Z.; Lu, P. Anti-resonant reflecting guidance in alcohol-filled hollow core photonic crystal fiber for sensing applications. *Opt. Lett.* **2013**, *21*, 31690–31697. [CrossRef]
45. Gao, R.; Lu, D.; Zhang, M.; Qi, Z. Optofluidic Immunosensor Based on Resonant Wavelength Shift of a Hollow Core Fiber for Ultratrace Detection of Carcinogenic Benzo[a]pyrene. *ACS Photonics* **2018**, *5*, 1273–1280. [CrossRef]
46. Zheng, D.; Cai, Z.; Floris, I.; Madrigal, J.; Pan, W.; Zou, X.; Sales, S. Temperature-insensitive optical tilt sensor based on a single eccentric-core fiber Bragg grating. *Opt. Lett.* **2019**, *44*, 5570–5573. [CrossRef] [PubMed]
47. Guo, K.; He, J.; Shao, L.; Xu, G.; Wang, Y. Simultaneous Measurement of Strain and Temperature by a Sawtooth Stressor-Assisted Highly Birefringent Fiber Bragg Grating. *J. Lightwave Technol.* **2020**, *38*, 2060–2066. [CrossRef]
48. Zuowei, X.; Huang, B.; Shu, X. Dual interference effects in a line-by-line inscribed fiber Bragg grating. *Opt. Lett.* **2020**, *45*, 2950–2953.
49. Zhang, S.; Li, X.; Niu, H.; Yan, Q.; Sun, C.; Peng, F.; Ma, Y.; Zhang, K.; Geng, T.; Yang, W.; et al. Few-mode fiber-embedded long-period fiber grating for simultaneous measurement of refractive index and temperature. *Appl. Opt.* **2020**, *59*, 9248–9253. [CrossRef] [PubMed]
50. Ni, W.; Lu, P.; Luo, C.; Fu, X.; Liu, L.; Jiang, X.; Liao, H.; Liu, D.; Zhang, J. Bending direction detective fiber sensor for dual-parameter sensing based on an asymmetrical thin-core long-period fiber grating. *IEEE Photonics J.* **2016**, *8*, 6803811. [CrossRef]
51. Gao, R.; Lu, D.; Cheng, J.; Jiang, Y.; Jiang, L.; Qi, Z. Optical displacement sensor in a capillary covered hollow core fiber based on anti-resonant reflecting guidance. *IEEE J. Sel. Top. Quantum Electron.* **2016**, *23*, 5600106. [CrossRef]
52. Gao, R.; Lu, D.; Cheng, J.; Qi, Z. In-Fiber Double-Layered Resonator for High-Sensitive Strain Sensing. *IEEE Photonics Technol. Lett.* **2017**, *29*, 857–860. [CrossRef]
53. Liu, S.; Tian, J.; Liu, N.; Xia, J.; Lu, P. Temperature Insensitive Liquid Level Sensor Based on Antiresonant Reflecting Guidance in Silica Tube. *J. Lightwave Technol.* **2016**, *34*, 5239–5243. [CrossRef]
54. Hou, M.; Zhu, F.; Wang, Y.; Wang, Y.; Liao, C.; Liu, S.; Lu, P. Antiresonant reflecting guidance mechanism in hollow-core fiber for gas pressure sensing. *Opt. Lett.* **2016**, *24*, 27890–27898. [CrossRef] [PubMed]
55. Liu, D.; Wu, Q.; Mei, C.; Yuan, J.; Xin, X.; Mallik, A.K.; Wei, F.; Han, W.; Kumar, R.; Yu, C.; et al. Hollow Core Fiber Based Interferometer for High-Temperature (1000 °C) Measurement. *J. Lightwave Technol.* **2018**, *36*, 1583–1590. [CrossRef]
56. Herrera-Piad, L.A.; Hernández-Romano, I.; May-Arrioja, D.A.; Minkovich, V.P.; Cisneros, M.T. Sensitivity Enhancement of Curvature Fiber Sensor Based on Polymer-Coated Capillary Hollow-Core Fiber. *Sensors* **2020**, *20*, 3763. [CrossRef]
57. Ni, W.; Lu, P.; Zhang, J.; Yang, C.; Fu, X.; Sun, Y.; Liao, H.; Liu, D. Single hole twin eccentric core fiber sensor based on anti-resonant effect combined with inline Mach-Zehnder interferometer. *Opt. Lett.* **2017**, *25*, 12372–12380. [CrossRef] [PubMed]
58. Jaworski, P.; Krzempek, K.; Dudzik, G.; Sazio, P.J.; Belardi, W. Nitrous oxide detection at 5.26 μm with a compound glass antiresonant hollow-core optical fiber. *Opt. Lett.* **2020**, *45*, 1326–1329. [CrossRef] [PubMed]
59. Nikodem, M.; Gomółka, G.; Klimczak, M.; Pysz, D.; Buczyński, R. Demonstration of mid-infrared gas sensing using an anti-resonant hollow core fiber and a quantum cascade laser. *Opt. Lett.* **2019**, *27*, 36350–36357. [CrossRef] [PubMed]
60. Jaworski, P.; Koziol, P.E.; Krzempek, K.; Wu, D.; Yu, F.; Boj, P.; Dudzik, G.; Liao, M.; Abramski, K.M.; Knight, J.C. Antiresonant Hollow-Core Fiber-Based Dual Gas Sensor for Detection of Methane and Carbon Dioxide in the Near-and Mid-Infrared Regions. *Sensors* **2020**, *20*, 3813. [CrossRef] [PubMed]
61. Zhao, P.; Zhao, Y.; Bao, H.; Ho, H.; Jin, W.; Fan, S.; Gao, S.; Wang, Y.; Wang, P. Mode-phase-difference photothermal spectroscopy for gas detection with an anti-resonant hollow-core optical fiber. *Nat. Commun.* **2020**, *11*, 847. [CrossRef]
62. Mona, N.; Brenda, D.; Jonas, H.; Jens, K.; Karina, W.; Thomas, H.; Maekus, A.S. UV Absorption Spectroscopy in Water-Filled Antiresonant Hollow Core Fibers for Pharmaceutical Detection. *Sensors* **2018**, *18*, 478.
63. Liu, X.; Ding, W.; Wang, Y.; Gao, S.; Cao, L.; Feng, X.; Wang, P. Characterization of a liquid-filled nodeless anti-resonant fiber for biochemical sensing. *Opt. Lett.* **2017**, *42*, 863–866. [CrossRef]

64. Adamu, A.I.; Wang, Y.; Correa, R.A.; Bang, O.; Markos, C. Low-loss micro-machining of anti-resonant hollow-core fiber with focused ion beam for optofluidic application. *Opt. Mater. Express* **2021**, *11*, 338–344. [CrossRef]
65. Qiao, P.; Wang, X.; Gao, S.; Yin, X.; Wang, Y.; Wang, P. Integration of black phosphorus and hollow-core anti-resonant fiber enables two-order magnitude enhancement of sensitivity for bisphenol A detection. *Biosens. Bioelectron.* **2019**, *149*, 111821. [CrossRef]
66. Sanders, G.A.; Taranta, A.A.; Narayanan, C.; Fokoua, E.N.; Mousavi, S.A.; Strandjord, L.K.; Smiciklas, M.; Bradley, T.D.; Hayes, J.; Jasion, G.T.; et al. Hollow-core resonator fiber optic gyroscope using nodeless anti-resonant fiber. *Opt. Lett.* **2021**, *46*, 46–49. [CrossRef]
67. Zhang, N.; Humbert, G.; Gong, T.; Shum, P.; Li, K.; Auguste, J.R.; Wu, Z.; Hu, J.; Luan, F.; Dinh, Q.; et al. Side-channel photonic crystal fiber for surface enhanced Raman scattering sensing. *Sens. Actuators B. Chem.* **2016**, *223*, 195–201. [CrossRef]
68. Zhang, M.; Li, K.; Shum, P.; Yu, X.; Zeng, S.; Wu, Z.; Wang, Q.; Yong, K.; Wei, L. Hybrid graphene/gold plasmonic fiber-optic biosensor. *Adv. Mater. Technol.* **2017**, *2*, 1600185. [CrossRef]
69. Zhang, M.; Li, K.; Zhang, T.; Shum, P.; Wang, Z.; Wang, Z.; Zhang, N.; Zhang, J.; Wu, T.; Wei, L. Electron-rich two-dimensional molybdenum trioxides for highly integrated plasmonic biosensing. *ACS Photonics* **2018**, *5*, 347–352. [CrossRef]
70. Zhang, N.; Humbert, G.; Wu, Z.; Li, K.; Shum, P.; Zhang, M.; Cui, Y.; Auguste, J.L.; Dinh, X.; Wei, L. In-line optofluidic refractive index sensing in a side-channel photonic crystal fiber. *Opt. Lett.* **2016**, *24*, 27674–27682. [CrossRef] [PubMed]
71. Zhang, N.; Li, K.; Cui, Y.; Wu, Z.; Shum, P.; Auguste, J.L.; Dinh, X.; Humbert, G.; Wei, L. Ultra-sensitive chemical and biological analysis via specialty fibers with built-in microstructured optofluidic channels. *Lab Chip* **2018**, *18*, 655–661. [CrossRef] [PubMed]
72. Zhang, M.; Qi, M.; Wang, Z.; Wang, Z.; Chen, M.; Li, K.; Shum, P.; Wei, L. One-step synthesis of cyclodextrin-capped gold nanoparticles for ultra-sensitive and highly-integrated plasmonic biosensors. *Sens. Actuators B. Chem.* **2019**, *286*, 429–436. [CrossRef]